nature physics

Article

https://doi.org/10.1038/s41567-026-03359-4

# Surface *d*-orbital order in an intermetallic compound

Received: 2 November 2025

Accepted: 3 June 2026

Published online: 29 June 2026

Check for updates

Zhanyang Hao[1,2,17], Haohao Sheng[3,4,17], Wanru Ma[5,6,17] ✉, Wengen Zheng[7,8,17], Yongqing Cai[9,17] ✉, Zijuan Xie[10,17], Wanlin Cheng[6], Zuowei Liang[6], Wu Xie[7,8], Wenjuan Zhao[8], Chen Liu[8], Zhibin Su[3], Junhao Lin[2], Liusuo Wu[2], Zhengtai Liu[11], Mao Ye[11], Ji Dai[12], Massimo Tallarida[12], Shengtao Cui[13], Yogendra Kumar[14], Kenya Shimada[14], Kenichi Ozawa[15], Shuki Torii[16], Kazuhiro Mori[16], Yue Xie[3,4], Junze Deng[3,4], Jiaou Wang[8], Xuetao Zhu[3], Jiandong Guo[3], Jiawei Mei[2], Zhenyu Wang[6] ✉, Xianhui Chen[6], Ping Miao[7,8] ✉, Zhijun Wang[3,4] ✉ & Chaoyu Chen[1,2] ✉

Orbital order describes a quantum state where occupied orbitals line up in a periodic pattern. Although orbital physics plays a fundamental and universal role in strongly correlated electron systems, the existence and particularly the band-structure fingerprint of orbital order remain a long-standing mystery. Here we report the discovery of rare earth 5*d*-orbital order developed by the surface states of the intermetallic compound $Tb_2CoAl_4Ge_2$. Angle-resolved photoemission spectroscopy reveals characteristic nematic features such as Fermi surface deformation and band splitting. These experimental observations can be described by a ferro-orbital order term in the mean-field Hamiltonian. The structural and magnetic origin of such order is excluded by systematic high-resolution neutron powder diffraction and scanning tunnelling microscopy measurements. Our results provide strong evidence for a pure surface orbital order scenario avoiding complications from structural distortion as in colossal magnetoresistance manganites, magnetic order as in iron-based superconductors and charge transfer *p*-orbital order in cuprates.

Complex solid-state systems are characterized by the synergy of lattice, charge, spin and orbital degrees of freedom, bridged through Coulomb repulsion, electron–phonon coupling, exchange, spin–orbit coupling and so on. Such synergy results into a wide range of macroscopic phenomena such as magnetism, superconductivity, nematicity, density waves and so on. Described as Landau's spontaneous symmetry-breaking phases, such quantum states of matter are accompanied or even characterized by orders of degree of freedom. For example, charge density wave, charge order, stripe phase and phase separation are dominated by the electronic charge degree of freedom. Similarly, spin density wave (SDW), magnetic order, spin fluctuation and skyrmions are rooted in the electronic spin. As the charge and spin manifest as macroscopically measurable quantities, their corresponding orders have been extensively studied, forming the frontiers of modern condensed matter physics.

The third electronic degree of freedom, orbital and its related quantum order, the orbital order, by contrast, remain largely unexplored, partially due to the lack of direct experimental probe. By definition, orbital order is a spontaneous symmetry-breaking state in which localized occupied orbitals line up in a periodic pattern, in a similar way as spins do in magnetically ordered structures. On one hand, orbital order is argued to play a fundamental role in shaping the phase diagram and colossal magnetoresistance[1–4] of manganites, the nematicity[5–15] and pseudogap phase[16–25] of high-$T_c$ superconductors. On the other hand, the dominant existence of orbital order has never been ascertained in strongly correlated electrons. For example, in perovskite manganites,

A full list of affiliations appears at the end of the paper. ✉e-mail: mwr19@mail.ustc.edu.cn; yqcai@dlut.edu.cn; zywang2@ustc.edu.cn; miaoping@ihep.ac.cn; wzj@iphy.ac.cn; chenchaoyu@sslab.org.cn

https://doi.org/10.1038/s41567-026-03359-4

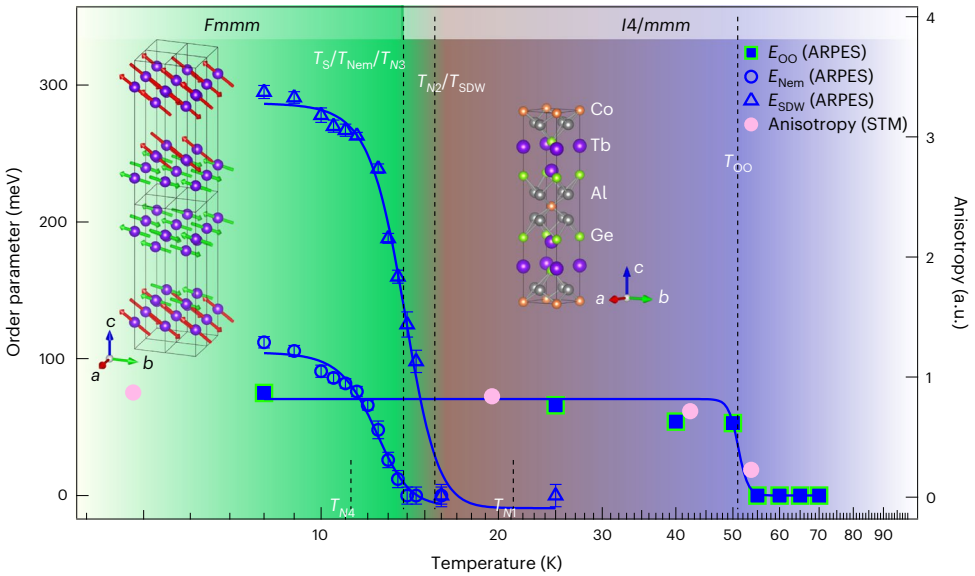


**Fig. 1 | Phase diagram of $Tb_2CoAl_4Ge_2$.** NPD, heat capacity and susceptibility measurements reveal four consecutive AFM transitions, at $T_{N1} = 21.2$ K, $T_{N2} = 15.6$ K, $T_{N3} = 13.8$ K and $T_{N4} = 11.24$ K, respectively. The insets illustrate the unit cell of magnetic lattice (left) and crystal lattice (right), determined by NPD and X-ray diffraction experiments. Blue symbols and lines are the order parameters, represented by the band splitting extracted from the measured ARPES spectra. The open triangles describe the SDW-like hybridization gap of one bulk band, defining an onset temperature $T_{SDW} = T_{N2} = 15.6$ K. Open circles represent the nematicity-like energy splitting between the Tb $5d_{xz}$ and $5d_{yz}$ bulk bands, manifesting an onset temperature $T_{Nem} = T_S = T_{N3} = 13.8$ K; here $T_S$ marks the structural phase transition between high-temperature tetragonal (*I*4/*mmm*) and low-temperature orthorhombic (*Fmmm*) phases, determined by high-resolution NPD experiments. The filled squares indicate the ferro-orbital order induced surface-state band anisotropy, with a phase transition temperature $T_{OO} \approx 51$ K. The pink-filled circles show the STM anisotropy ratio (amplitude ratio at the lattice wave vector) as a function of temperature, which is significantly suppressed near $T_{OO}$, consistent with the ARPES results. The error bars of $E_{SDW}$ and $E_{Nem}$ represent the standard deviation of the Lorentzian fits to the energy distribution curve peaks in Supplementary Figs. 11 and 12, respectively.

electronic orbital ordering and structural Jahn–Teller distortion are concurrent[26], rendering it difficult to distinguish the driving force between Kugel–Khomskii superexchange orbital order[27,28] and Kanamori electron–phonon coupling[29]. In iron-based superconductors, orbital order is theoretically proposed to account for the nematicity, the structural phase transition and the resistivity anomaly[30–36]. Unfortunately, its existence is challenged by the momentum dependence and sign reversal of band splitting[37,38], as directly revealed by angle-resolved photoemission spectroscopy (ARPES). Moreover, inelastic neutron scattering results[11,15] strongly suggest the spin fluctuation-driven nematicity scenario[39,40]. In cuprates, nematicity emerges at the onset of pseudogap phase[16–24], with signature of orbital order from O 2*p*, rather than Cu 3*d*, due to charge transfer superexchange[25]. By and large, orbital physics has its ubiquitousness in 3*d* strongly correlated electron systems[26,41,42]. Paradoxically, orbital order and its band spectral signature lack definitive recognition, let alone its existence in 4*d* and 5*d* systems with extended wave functions.

Here we substantiate the existence of 5*d*-orbital order by illustrating its clear band-structure character, Fermi surface deformation and orbital polarization in rare earth intermetallic alumogermanide $Tb_2CoAl_4Ge_2$. As shown in the phase diagram in Fig. 1, bulk $Tb_2CoAl_4Ge_2$ crystals undergo paramagnetic–antiferromagnetic (AFM) ($T_{N1}$) and several AFM transitions ($T_{N2}$, $T_{N3}$ and $T_{N4}$) at 10 K < $T$ < 22 K. The high-temperature tetragonal-to-low-temperature orthorhombic structural transition ($T_S$) accompanies the spin reorientation transition ($T_{N3}$) and nematicity-like bulk band splitting ($T_{Nem}$). The AFM transition $T_{N2}$ occurs with SDW-like bulk band folding and hybridization gap ($T_{SDW}$). These bulk band features are all captured by density functional theory (DFT) calculations in a single-particle picture.

Our key discovery comes from the ARPES observed surface states, which develop ferro-orbital order and resultant spontaneous tetragonal symmetry breaking at temperature well above the bulk AFM and structural transition, that is, $T_{OO} \approx 51$ K $\gg T_{N1} = 21.2$ K $> T_S = 13.8$ K. Scanning tunnelling microscopy (STM) and DFT analyses attribute these surface states to the surface Tb atoms, with $5d_{xz}/d_{yz}$ orbital origin. Temperature-dependent ARPES measurements uncover a surface-state nematic transition at $T_{OO}$, characterized by Fermi surface deformation and band splitting in the band structure, which is further supported by the $C_2$-symmetric spectroscopic mapping within one unit cell and quasi-particle interference in a relevant energy window of the surface state. We also notice nematic domains whose preferential orientations are perpendicular to each other, suggesting the spontaneous symmetry-breaking nature. Moreover, no visible structural distortion has been found with high-resolution low-energy electron diffraction (LEED) and STM topographic images on the surface. We model the surface state by constructing a mean-field Hamiltonian containing Pomeranchuk instability and ferro-orbital order interactions. The ferro-orbital order term leads to orbital-dependent band splitting, decently reproduces the ARPES features. Such orbital order scenario is further validated by the uniform surface-state orbital polarization observed in linear dichroism (LD)-ARPES. Altogether, our observations establish the emergence of orbital order from rare earth 5*d* electrons, with its existence avoiding the entanglement with the structural distortion as in the colossal magnetoresistance manganites[26] and the AFM order as in the iron-based superconductors[39,40]. Its *d*-orbital origin also distinguishes itself from the *p*-orbital order in cuprates[25], symbolizing pure, strongly correlated orbital physics[41].

## Magnetic, structural, symmetry and bulk band evolution

At room temperature, rare earth intermetallic alumogermanide $Tb_2CoAl_4Ge_2$ crystallizes in a tetragonal structure with space group *I*4/*mmm* (ref. 43) (number 139; Supplementary Fig. 1 and Supplementary Table 1). As temperature decreases, $Tb_2CoAl_4Ge_2$ experiences four consecutive magnetic transitions, which are determined

mainly from the intensity change of magnetic Bragg peaks in neutron powder diffraction (NPD) experiments (Supplementary Figs. 2 and 3 and Extended Data Fig. 1) and corroborated by the slope change of heat capacity and susceptibility (Extended Data Fig. 2 and Supplementary Fig. 4). Curie–Weiss fit of susceptibility (Supplementary Fig. 4) for 300 K > $T$ > 50 K yields effective moment ~ 10 $\mu_B$ (Bohr magneton), close to the theoretical value of $Tb^{3+}$. This suggests no moment contribution from Co atoms, which is also confirmed by the magnetic structure analysis on the NPD data (Extended Data Fig. 1, Supplementary Fig. 5 and Supplementary Tables 3–6) and related works[44]. The paramagnetic–AFM transition occurs at $T_{N1} = 21.2$ K, indicated by the appearance of a new magnetic Bragg peak in NPD patterns (Supplementary Fig. 2) and slope change in heat capacity (Extended Data Fig. 2) but no clear feature from susceptibility and band structure, probably due to the small magnitude of ordered moments (Extended Data Fig. 1 and Supplementary Table 3). As shown in Supplementary Fig. 1 and Extended Data Fig. 1, the magnetic unit cell of AFM1 is 2 × 2 of the tetragonal crystal unit cell and the moments have components along the $a$, $b$ and $c$ axes, with $m_a = m_b \gg m_c$ (Supplementary Table 3). The magnetic unit cell further doubles itself along the $c$ axis (now 2 × 2 × 2) when entering AFM2 at $T_{N2} = 15.6$ K, with enlarged moments for the $c$ component (Extended Data Fig. 1 and Supplementary Table 4). Such enlargement validates the magnetic effect on the ARPES observed band structure, manifested as SDW-like bulk band folding and hybridization gap $E_{SDW}$ (Fig. 1, $T_{SDW} = T_{N2}$). The major AFM transition dominating the heat capacity and susceptibility curves (Extended Data Fig. 2) occurs at $T_{N3} = 13.8$ K, accompanied by spin reorientation (AFM3, Extended Data Fig. 1) and concurrent tetragonal-to-orthorhombic crystal structure transition ($T_S$, Supplementary Fig. 1) detected by high-resolution NPD. Note that the orthorhombic distortion at $T_S$ is too weak to be detected by X-ray diffraction (Supplementary Fig. 6). The orthorhombic crystal structure below $T_S$ is well described by one of the maximal subgroups of $I4/mmm$, space group $Fmmm$ (number 69, Supplementary Fig. 1 and Supplementary Table 2). Similar to the nematic phase transition in iron-based superconductors[39,40], the bulk $d_{xz}/d_{yz}$ bands split in energy ($E_{Nem}$) at this temperature, defining a nematicity-like transition with $T_{Nem} = T_S = T_{N3}$. Note that the crystal structure transition not only reduces the in-plane $C_4$ symmetry to $C_2$ but also expands the unit cell approximately to $\sqrt{2} \times \sqrt{2}$ with rotation 45° relative to the tetragonal one (Supplementary Fig. 1 and Supplementary Table 2). On further cooling, the moments reorient again at $T_{N4} = 11.24$ K (Extended Data Fig. 1 and Supplementary Table 6), with simultaneous saturation behaviour of the SDW-like hybridization gap $E_{SDW}$ and nematicity-like band splitting $E_{Nem}$ (Fig. 1). The nature of these two energy order parameters shall be discussed in the following.

Photon energy-dependent spectral mappings (Supplementary Fig. 7) exhibit no clear dispersion along $k_z$, suggesting overall two-dimensional electronic structure, in line with the layered lattice structure. We thus only discuss the electronic structure in the cleaved $ab$ plane. As shown in Fig. 2, the low-energy electronic states of $Tb_2CoAl_4Ge_2$ consist of steeply dispersed band manifolds around the Brillouin zone (BZ) centre Γ (Fig. 2a,c), and several electron-type bands enclosing the BZ corner M points (Fig. 2a,b). In the present work, we concentrate on these M-region bands, including two parabolic ones with deep bottoms at ~−0.8 eV and one W-shaped band with shallow bottoms at ~−0.25 eV (Fig. 2b, left). According to our DFT calculations (Supplementary Figs. 8 and 9), the formers are bulk conduction bands (BCBs), whereas the latter is surface state residing on the double-Tb-layer termination, both from Tb $5d_{xz}/d_{yz}$ orbitals. To verify this assignment, spatially resolved X-ray photoelectron spectroscopy (XPS) and ARPES measurements are conducted (Extended Data Fig. 3). XPS mapping reveals two types of regions with distinct core-level signatures, corresponding to the Tb1 and Tb2 terminations illustrated in Fig. 4b. ARPES results confirm that only the Tb1 termination hosts the characteristic W-shaped surface state near the M point, in excellent agreement with DFT calculations (Supplementary Fig. 9).

The constant energy contours at various binding energies and high-symmetry-path spectra measured at 7 K (Fig. 2a–c) exhibit tetragonal symmetry breaking for both bulk and surface bands. At high binding energy 1.0 eV (Fig. 2a, left), the bulk valence bands obey the in-plane $C_4$ symmetry. Moving to $E_F$ (Fig. 2a, right), the BCBs break the $C_4$ symmetry by developing band folding features with respect to the orthorhombic BZ border (dashed white lines). The main and folded outer BCBs hybridize at this border, which is the middle point of Γ − M1 of the tetragonal BZ and open an SDW-type gap ($E_{SDW}$; Fig. 2c, left). On the contrary, along Γ − M2 the folding and gap cannot be resolved in ARPES spectra (Fig. 2c, right), which is attributed to the minute gap size according to DFT calculation (Supplementary Fig. 10). We also observe band splitting between the $5d_{xz}/d_{yz}$ BCBs along Γ − M1/M2, reminiscent of the $3d_{xz}/d_{yz}$ nematic splitting in Fe-based superconductors[38], thus defining an order parameter $E_{Nem}$.

The evolution of order parameters $E_{Nem}$ and $E_{SDW}$ with temperature can be tracked by measuring their magnitudes in temperature-dependent ARPES spectra. As shown in Fig. 2d, at temperature $T_{N3} < T = 14$ K $< T_{N2}$, $E_{SDW}$ reduces significantly but remains visible, yet $E_{Nem}$ vanishes. Systematic temperature-dependent analyses in Supplementary Figs. 11 and 12 show that $E_{SDW}$ appears below 16 K, with estimated $T_{SDW} = T_{N2} = 15.6$ K. $E_{Nem}$ emerges with the onset of AFM3 and structural transition, that is, $T_{Nem} = T_S = T_{N3}$, again, imitating the magneto-elastic coupling and nematicity in some iron-based superconductors[39,40]. Nevertheless, the behaviours of $E_{SDW}$ and $E_{Nem}$ can be reproduced in our DFT calculation (Supplementary Fig. 10) by including the corresponding magnetic structure, suggesting AFM origin of the bulk band $C_4$ symmetry breaking.

## Surface ferro-orbital order and orbital polarization

The surface states manifest distinct symmetry breaking at low temperature with elongated Fermi surfaces along X − M1 (Figs. 2a and 3d). We construct a Wannier tight-binding model from the non-magnetic calculations, then use an iterative method to obtain the surface Green's function of the semi-infinite system. The experiment surface is found to be terminated on the 2-Tb layers (Supplementary Fig. 9). The corresponding Fermi surface projections present surface-state contours resembling the 'Chinese knot' (Supplementary Fig. 9c). In general, the bulk and surface Fermi surface projections (Supplementary Fig. 9c,f) are consistent with the ARPES results (Fig. 3b, 60 K).

To simulate the evolution of surface states, we build a two-orbital minimal model, which reads,

$$H_0(k_x,k_y) = m\sigma_0 + A(k_x,k_y)\sigma_0 + B(k_x,k_y)\sigma_z + C(k_x,k_y)\sigma_x, \quad (1)$$

with $A(k_x,k_y) = t_1\left(k_x^2+k_y^2\right) + t_1'\left(k_x^4+k_y^4\right) + t_1''k_x^2k_y^2$, $B(k_x,k_y) = t_2\left(k_x^2-k_y^2\right) + t_2'\left(k_x^4-k_y^4\right)$ and $C(k_x,k_y) = t_3k_xk_y + t_3'\left(k_x^3k_y + k_xk_y^3\right)$. The two orbitals retained in our minimal model are the Tb $d_{xz}$ and $d_{yz}$ orbitals. Such a two-dimensional model can reproduce the DFT surface band structure and $C_{4v}$ symmetry well (see Supplementary Fig. 13 and Supplementary Table 7 for the parameters and results). As shown in Fig. 3a, the two surface-state bands degenerate at $\overline{M}$ point and the Fermi surfaces present 'Chinese knot' contours with $C_4$ symmetry, capturing the ARPES observed features at 60 K (Fig. 3b).

Regarding surface-state symmetry breaking, we consider the following interaction Hamiltonian

$$H_{int} = \frac{S}{2(2\pi)^2}\iint d^2k\,d^2k'\left[f_{kk'}n_k^+n_{k'}^+ - vn_k^-n_{k'}^-\right]. \quad (2)$$

Here, $f_{kk'} = -gd_kd_{k'}$ and $d_k = k_x^2 - k_y^2$. $n_k^\pm = n_{xk} \pm n_{yk}$. $S$ is the area of the unit cell. $g$ and $v$ are the interaction strengths. $n_{xk}$ and $n_{yk}$ are

https://doi.org/10.1038/s41567-026-03359-4

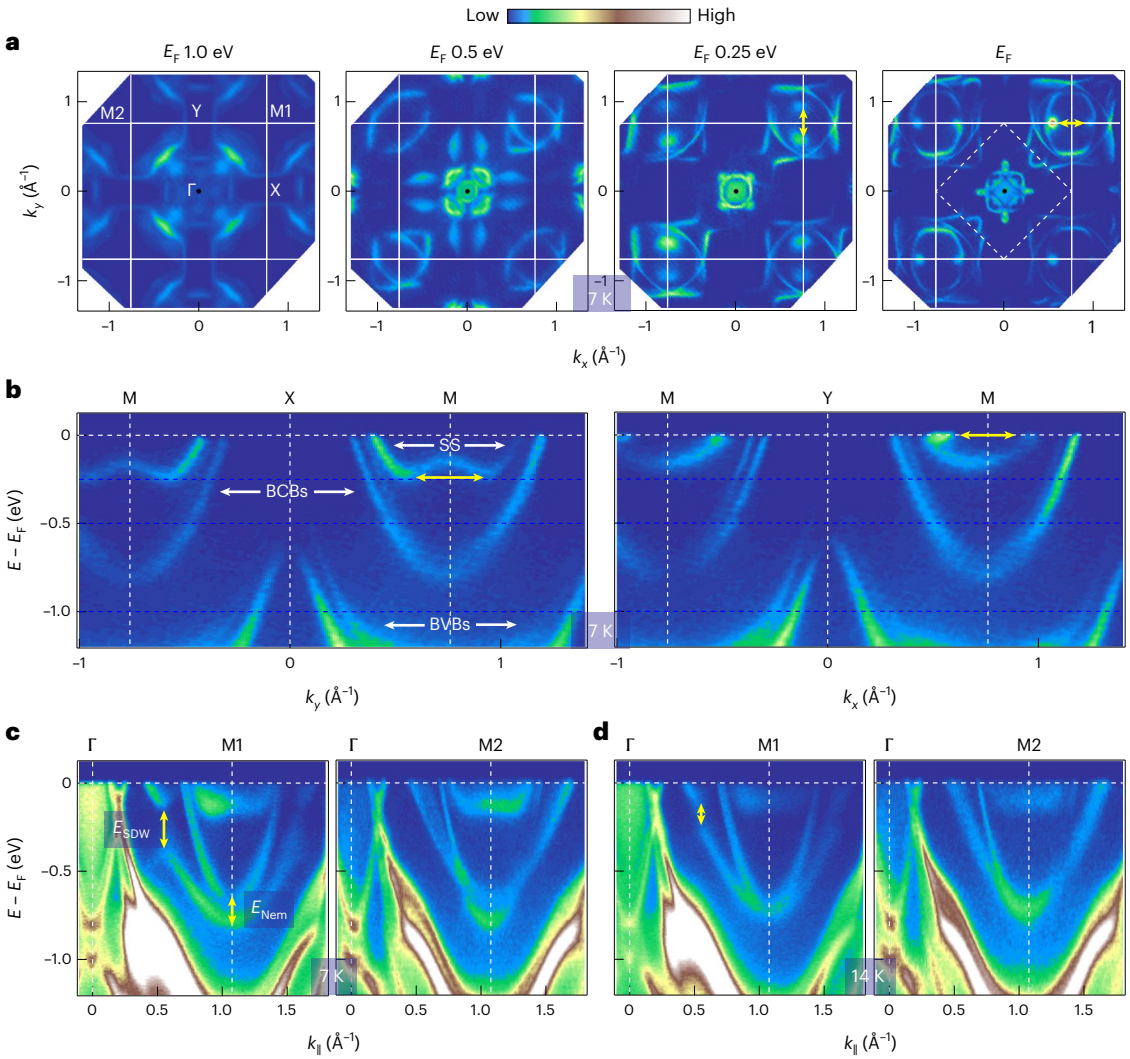


**Fig. 2 | Orientation dependent $C_4$ symmetry breaking of surface and bulk electronic states. a**, ARPES spectral intensity in $k_x - k_y$ space at various constant energies. The solid white lines and characters indicate the high-temperature tetragonal BZ boundaries and high-symmetry points. The dashed white lines represent the low-temperature orthorhombic BZ. **b**–**d**, ARPES band spectra along M–X(Y)–M (**b**), Γ–M1/M2 at 7 K (**c**) and Γ–M1/M2 at 14 K (**d**). The white arrows and acronyms in **b** show the assignment of surface state (SS), BCBs and bulk valence band (BVBs). The horizontal yellow arrows in **b** highlight the bottom of the W-shaped surface bands. The vertical yellow arrows in **c** illustrate the order parameters $E_{SDW}$ and $E_{Nem}$, defined as the corresponding band energy split. All the ARPES results here are measured with photon energy 119 eV, at sample temperatures 7 K for **a**–**c** and 14 K for **d**, respectively. $E_F$, Fermi level.

density operators of $d_{xz}$ and $d_{yz}$ orbitals, respectively. In equation (2), the first term corresponds to Pomeranchuk instability via forward-scattering interaction[45,46], whereas the second term represents ferro-orbital order from Kugel–Khomskii interaction[47,48] at mean-field level without magnetization. Then, we solve the total Hamiltonian $H_0 + H_{int}$ by the Hartree–Fock mean-field method (see the Methods for details). Without loss of generality, we consider the two orderings individually. The results of *d*-wave Pomeranchuk instability are shown in Supplementary Fig. 13, whose Fermi surfaces are still Chinese-knot-like with weak $C_4$ breaking.

The results of the ferro-orbital order (Fig. 3c) can explain the low-temperature ARPES data (Fig. 3d) very well. First, the double degeneracy of surface bands at $\overline{M}$ is lifted. Second, the $C_4$ symmetry is broken clearly from the simulated dispersions along $\overline{M} - \overline{X}$ and $\overline{M} - \overline{Y}$. Third, the constant energy contours decently reproduce the ARPES Fermi surface. Particularly, the two point-shaped features come from the bottoms of the W-shaped band located slightly above the Fermi level. Based on these agreements, we conclude that the surface-state nematic symmetry breaking originates from the ferro-orbital order in $Tb_2CoAl_4Ge_2$. The inclusion of spin–orbit coupling in our mean-field calculations does not alter the conclusion that ferro-orbital order is responsible for the observed $C_4$ symmetry breaking (Extended Data Fig. 4).

We trace the ferro-orbital order transition through the temperature dependence of surface states. As shown in Fig. 3b,d and Extended Data Fig. 5, Fermi surfaces remain elongated up to 50 K and regain the $C_4$ symmetry only reaching 60 K. At 8 K (Fig. 3d and Extended Data Fig. 5b, top), the surface spectra along $k_y$ is W-shaped, with global band peak minima at ~−0.22 eV and local maxima (M point) at ~−0.14 eV. Changing to $k_x$, it is U-shaped with minima at ~−0.14 eV, suggesting a saddle point formed at M. At 60 K, the spectral anisotropy disappears (Fig. 3b and Extended Data Fig. 5b, bottom). Defining the energy difference between the W–U band minima as the ferro-orbital order parameter $E_{OO}$, we track its temperature evolution (Extended Data Figs. 5d,e). To confirm the reproducibility of this transition, we performed the temperature-dependent ARPES measurements on another sample (Supplementary Fig. 14). As summarized in Fig. 1, $E_{OO}$ sets on roughly at ~ 51 K, more than twice higher than the bulk AFM and structure transition, $T_{OO} \approx 51\,K \gg T_{N1} = 21.2\,K > T_S = 13.8\,K$ , suggesting the ferro-orbital order is decoupled from the bulk AFM order and orthorhombic structure transition.

https://doi.org/10.1038/s41567-026-03359-4

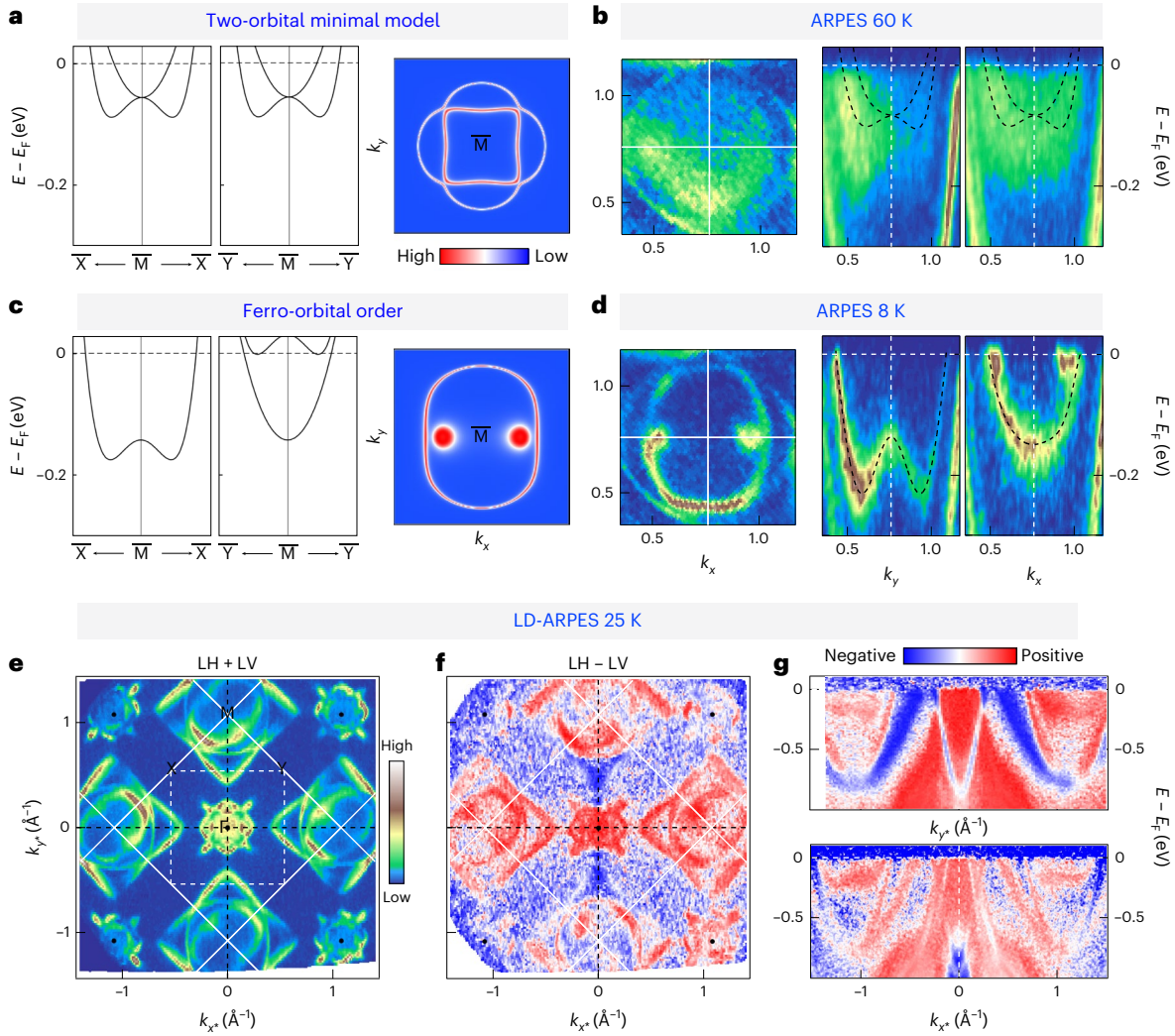


**Fig. 3 | Surface ferro-orbital order characterized by Fermi surface deformation, nematic orbital split and orbital polarization. a**,**c**, Results of two-orbital minimal model; surface-state energy bands and Fermi surface near $\overline{\mathrm{M}}$ point calculated from the model without (**a**) and with (**c**) ferro-orbital order. $v = 0.36$ eV and $g = 0$. **b**,**d**, Corresponding ARPES results; Fermi-surface and surface-state spectra overlaid with extracted dispersions (dashed black lines) measured at sample temperature 60 K (**b**) and 8 K (**d**). **e**, ARPES Fermi surface integrating photoemission intensity from photons with LH and LV polarization. We use the low-temperature orthorhombic BZ notations. **f**, LD Fermi surface. **g**, Corresponding LD spectra along $k_{y*}$ (top) and $k_{x*}$ (bottom) directions. Sample temperature is 25 K.

Analogous to spin polarization as the characteristic of ferromagnetic order, orbital polarization directly evidences ferro-orbital order[3,5]. We employ orbital sensitive LD-ARPES, in which the selection rules demand simultaneous odd or even symmetry with respect to the mirror plane for initial state orbitals and beam polarization vector. Here we switch to the orthorhombic BZ notations, in which $x^*z^*$ and $y^*z^*$ define the mirror planes. Shown in Fig. 3e,f are the sum and difference, respectively, of the Fermi surfaces mapped using linear horizontal (LH) and linear vertical (LV) polarization. In the LH + LV Fermi surface (Fig. 3e), spectral intensity of the main features obeys the $C_4$ rotation symmetry, whereas in the LD (LH − LV, Fig. 3f) Fermi surface, the outer BCBs surrounding M points show negative dichroism along $k_{y*}$, suggesting $d_{xz}$ orbital which is odd to the $y^*z^*$ measurement plane. Conversely, along $k_{x*}$, the dichroism is positive, suggesting $d_{yz}$ orbital. Although dichroism signals can in principle be influenced by matrix-element effects, the observed pattern remains unchanged under variations of photon energy and sample azimuth (Extended Data Fig. 6), making a matrix-element artefact highly unlikely. Such $d$-wave orbital polarization in reciprocal space is reminiscent of the spin polarization in our recently discovered $d$-wave altermagnet[49]. Whether a $d$-wave alter-orbital order exists and its relevant physics remain to be explored.

As expected, the surface-state bands and Fermi surfaces show uniform positive dichroism spanning the whole reciprocal space, suggesting dominant $5d_{yz}$ orbital occupation and full orbital polarization. As the sample is in the paramagnetic phase (25 K) for LD-ARPES, such orbital polarization is uniquely associated to and serving as a direct physical consequence of the surface ferro-orbital order.

## Surface intra-unit-cell orbital order

To further validate the origin of the surface states and the ferro-orbital order induced nematicity, we employ spectroscopic-imaging STM, which detects electronic wave function in real and reciprocal space simultaneously. Structurally, $Tb_2CoAl_4Ge_2$ crystals could cleave between either adjacent Ge and Tb layers or two Tb layers, exposing two types of Tb terminations (Fig. 4b, Tb1 and Tb2). Figure 4a shows the typical atom-resolved topography achieved from four cleaved samples; a comparison of the relative heights of multiple consecutive steps in a larger field of view (FOV, Fig. 4b) to the schematic crystal structure suggests that the large and flat surfaces are the Tb1 terminations.

https://doi.org/10.1038/s41567-026-03359-4

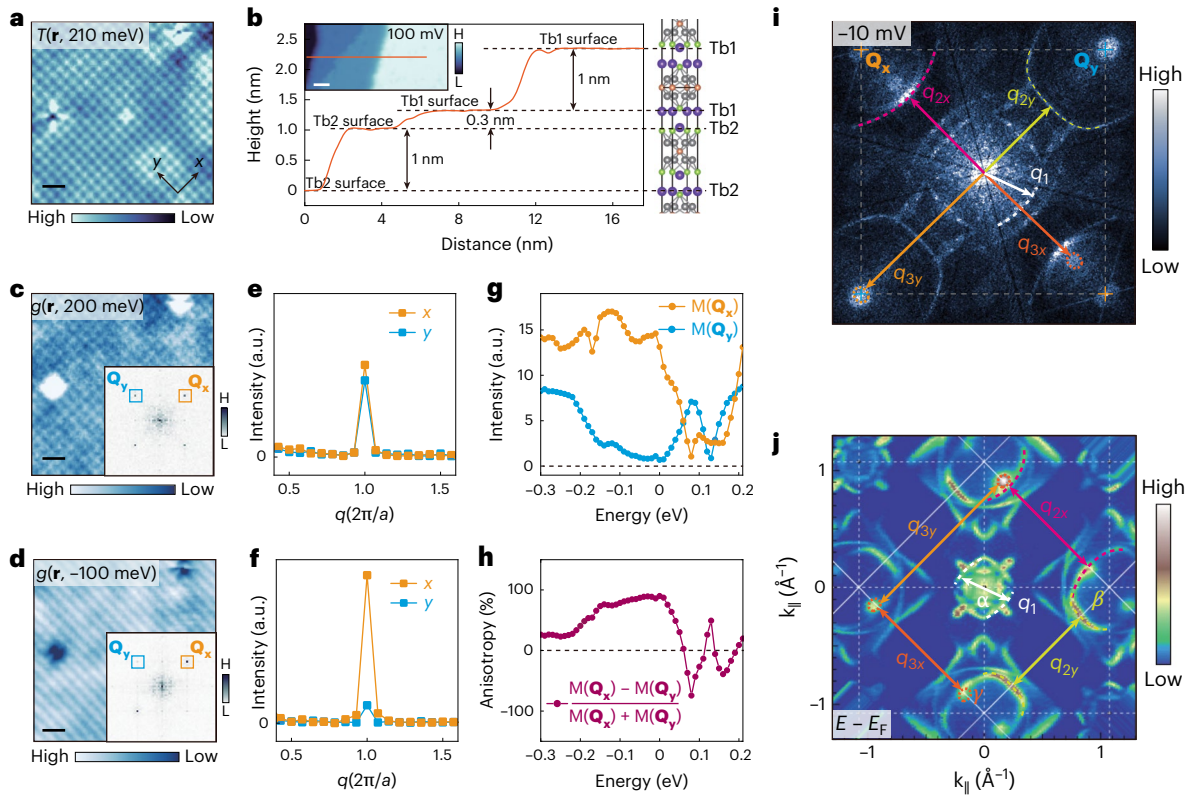


**Fig. 4 | Surface electronic nematicity originated from the Tb termination of $Tb_2CoAl_4Ge_2$.** **a**, Atomically resolved topographic image. **b**, Height profile obtained along the orange line in the inset (STM topography) showing that the main cleavage planes are Tb1 terminations. **c**,**d**, Typical d*I*/d*V* map acquired at 200 meV (**c**) and −100 meV (**d**) from the FOV in **a**. The inset shows the corresponding FT. **e**,**f**, FT linecuts along the lattice direction from the inset of **c** (**e**) and **d** (**f**), respectively. **g**, The intensity of atomic lattice in the FT, M($\mathbf{Q}_x$) and M($\mathbf{Q}_y$), as a function of energy (STM bias). **h**, Anisotropy ratio of the intensities $Z(eV)$. **i**, The quasi-particle interference pattern showing multiple scattering features, labelling wave vectors as coloured arrows along $\mathbf{Q}_x$ and $\mathbf{Q}_y$. **j**, Fermi surface map. The coloured double arrows indicate the corresponding scattering patterns in **i**. Setup conditions: sample bias $V_S$ = 210 mV, tunnelling current $I_t$ = 4 nA for **a**, $V_S$ = 100 mV, $I_t$ = 600 pA for **b**, inset, $V_S$ = 200 mV, $I_t$ = 4 nA, bias modulation $V_m$ = 4 mV for **c**, $V_S$ = −100 mV, $I_t$ = 4 nA, $V_m$ = 4 mV for **d**. Scale bars, 1 nm for **a**, **c** and **d**; 3 nm for **b**, inset.

This is further supported by our DFT calculations (Supplementary Fig. 9). Interestingly, the topographic images obtained at positive biases exhibit a marked $C_4$-symmetric square lattice of Tb atoms, and we did not find any notable structural distortion of the surface Tb atoms in neither the LEED pattern nor with supercell averaging algorithm for these topographic STM images (Supplementary Figs. 15–18). However, a striped pattern appears at negative biases, breaking the $C_4$ symmetry (Supplementary Fig. 19). As a topographic image contains convoluted information on both lattice corrugation and electronic density modulation, and the former is, in principle, independent of the tunnel bias, the observed striped pattern is most likely to be a manifestation of rotation symmetry breaking of the underlying electronic state.

To get a clearer picture of any such electronic order, we image the energy-resolved local density of states $g(\mathbf{r}, \mathrm{eV})$ in the same FOV as Fig. 4a. Figure 4c,d displays two representative examples at 200 and −100 meV, respectively, with their Fourier transforms (FT) shown in the insets. Again, the electronic modulation seen in $g(\mathbf{r}, 200\ \mathrm{meV})$ is rather $C_4$-symmetric with roughly equal intensities at Bragg wave vectors $\mathbf{Q}_x = (\pm1, 0)2\pi/a$ and $\mathbf{Q}_y = (0, \pm1)2\pi/a$ (Fig. 4e). Contrarily, $g(\mathbf{r}, -100\ \mathrm{meV})$ clearly demonstrates a unidirectional modulation along one of the two lattice directions, and its FT (Fig. 4d, inset) exhibits inequivalent intensities at $\mathbf{Q}_x$ and $\mathbf{Q}_y$ (Fig. 4f). Tracking the intensity of the Bragg peaks as a function of energy, we find the peak amplitudes exhibit a markedly different energy dependence (Fig. 4g). We define a normalized order parameter, $Z(\mathrm{eV}) = (\mathrm{M}(\mathbf{Q}_y) - \mathrm{M}(\mathbf{Q}_x))/(\mathrm{M}(\mathbf{Q}_y) + \mathrm{M}(\mathbf{Q}_x))$ to measure the anisotropy of electronic modulations between $\mathbf{Q}_x$ and $\mathbf{Q}_y$. The plot of $Z$(eV) in Fig. 4h reveals prominent anisotropy in the bias window of −0.25–0.05 V, matching the surface-state energy range. This symmetry breaking is further corroborated by the energy-dependent spectral differences between inequivalent *x* and *y* bond centres (Extended data Fig. 7). Besides, electronic states near impurities exhibit a consistent $C_2$ symmetry that aligns with the global orientation of the striped modulation within a single domain (Extended data Fig. 8). Crucially, across the domain boundary, both the striped patterns and the local impurity states rotate by 90° on the same surface, excluding the STM tip anisotropy and local strain effect as possible origin of this $C_2$ modulation. Interestingly, such stripe pattern in fact gradually recovers to the square lattice of Tb atoms with $C_4$ symmetry above 51 K (Extended data Fig. 9), in good agreement with the ARPES data. These findings are a strong indicator that the electronic states on the Tb1 terminations spontaneously break the $C_4$ symmetry at low temperatures.

Correspondingly, the electronic structure in reciprocal space should also exhibit $C_4$ symmetry breaking at the same energy scale. To test this assumption, we study the electronic band structure through quasi-particle interference imaging. Figure 4i shows the FT of a selected image from normalized conductance maps at −10 mV obtained in a larger FOV, in which a rich array of scattering events can be identified with a comparison with the ARPES Fermi surface (Fig. 4j). Although the intra-band scattering of bulk $\alpha$ pocket preserves $C_4$ symmetry, the surface related scattering patterns develop clear nematicity. As shown by the coloured arrows, the arc features ($\mathbf{q}_2$) come from scattering between the elliptical surface-state Fermi surfaces, whereas point features ($\mathbf{q}_3$) connects the bright points formed by the bottoms of one

surface band, which is pushed up over the Fermi level by the ferro-orbital order (Fig. 2b). Both $\mathbf{q}_2$ and $\mathbf{q}_3$ are anisotropic between $\mathbf{Q}_x$ and $\mathbf{Q}_y$ direction, while $\mathbf{q}_1$, scattering between intra-band bulk Fermi surfaces, is $C_4$ symmetric. These results not only establish an intra-unit-cell electronic nematicity free from any bulk lattice distortion but also attribute such spontaneous nematic symmetry breaking to the surface ferro-orbital order.

## Discussion

In strongly correlated 3*d*-electron systems, orbital order has been long proposed to account for or be intimately related to a cascade of phenomena such as Verwey transition[42,50,51], cooperative Jahn–Teller distortion[52,53], colossal magnetoresistance[1,2,4], nematicity[30–36] and the pseudogap phase[25]. Nevertheless, the decisive fingerprint of orbital order is unclear. The reasons are twofold. In essence, orbital is frequently entangled with lattice, charge and spin degrees of freedom, so that the development of one order immediately induces the others, making the origin of such spontaneous symmetry breaking a physics realization of the 'chicken and egg problem'[26,39,40]. Methodologically, unlike spin and charge orders which are accessible directly via magnetization or polarization, there lacks an acknowledged approach to identify the characteristic of orbital order. Intuitively, the ordering temperature of the orbital we observed here is more than twice higher than that of AFM and structural distortion, distinguishing dominant orbital physics. Its 5*d*-orbital origin also expanding the arena where correlated orbital physics could emerge. On a deeper level, we have pointed out not only the electronic features of orbital order as Fermi surface deformation and band orbital splitting in ARPES but also the unique orbital polarization is revealed via LD-ARPES. Furthermore, spatial resolved ARPES uncovers nematic domains with preferential orientation parallel for the bulk states but mutually orthogonal for the surface states (Extended Data Fig. 10), in line with the topographic imaging of domain patterns (Extended Data Fig. 8), confirming the spontaneous symmetry breaking nature of surface orbital order. Notably, the $C_2$ electronic state is found to be insensitive to external magnetic field, providing robust evidence for an orbital-driven symmetry-breaking scenario (Supplementary Figs. 20–21). These approaches, combining different facets of ARPES functionality, set a new benchmark against which one can measure the intricate role that orbital physics is playing in a variety of phenomena through its strong coupling with charge, spin and lattice dynamics.

## Online content

Any methods, additional references, Nature Portfolio reporting summaries, source data, extended data, supplementary information, acknowledgements, peer review information; details of author contributions and competing interests; and statements of data and code availability are available at https://doi.org/10.1038/s41567-026-03359-4.

## References


1. van den Brink, J., Khaliullin, G. & Khomskii, D. Charge and orbital order in half-doped manganites. *Phys. Rev. Lett.* **83**, 5118–5121 (1999).
2. Mahadevan, P., Terakura, K. & Sarma, D. D. Spin, charge, and orbital ordering in $La_{0.5}Sr_{1.5}MnO_4$. *Phys. Rev. Lett.* **87**, 066404 (2001).
3. Huang, D. J. et al. Orbital ordering in $La_{0.5}Sr_{1.5}MnO_4$ studied by soft X-ray linear dichroism. *Phys. Rev. Lett.* **92**, 087202 (2004).
4. Yin, W.-G., Volja, D. & Ku, W. Orbital ordering in $LaMnO_3$: electron–electron versus electron–lattice interactions. *Phys. Rev. Lett.* **96**, 116405 (2006).
5. Occhialini, C. A. et al. Spontaneous orbital polarization in the nematic phase of FeSe. *Nat. Mater.* **22**, 985–991 (2023).
6. Zhao, J. et al. Spin waves and magnetic exchange interactions in $CaFe_2As_2$. *Nat. Phys.* **5**, 555–560 (2009).
7. Chu, J.-H. et al. In-plane resistivity anisotropy in an underdoped iron arsenide superconductor. *Science* **329**, 824–826 (2010).
8. Chuang, T. M. et al. Nematic electronic structure in the 'parent' state of the iron-based superconductor $Ca(Fe_{1-x}Co_x)_2As_2$. *Science* **327**, 181–184 (2010).
9. Chu, J.-H., Kuo, H.-H., Analytis, J. G. & Fisher, I. R. Divergent nematic susceptibility in an iron arsenide superconductor. *Science* **337**, 710–712 (2012).
10. Kasahara, S. et al. Electronic nematicity above the structural and superconducting transition in BaFe2$(As_{1-x}P_x)_2$. *Nature* **486**, 382–385 (2012).
11. Lu, X. et al. Nematic spin correlations in the tetragonal state of uniaxial-strained $BaFe_{2-x}Ni_xAs_2$. *Science* **345**, 657–660 (2014).
12. Baek, S. H. et al. Orbital-driven nematicity in FeSe. *Nat. Mater.* **14**, 210–214 (2015).
13. Glasbrenner, J. K. et al. Effect of magnetic frustration on nematicity and superconductivity in iron chalcogenides. *Nat. Phys.* **11**, 953–958 (2015).
14. Wang, F., Kivelson, S. A. & Lee, D.-H. Nematicity and quantum paramagnetism in FeSe. *Nat. Phys.* **11**, 959–963 (2015).
15. Wang, Q. et al. Strong interplay between stripe spin fluctuations, nematicity and superconductivity in FeSe. *Nat. Mater.* **15**, 159–163 (2016).
16. Tranquada, J. M., Sternlieb, B. J., Axe, J. D., Nakamura, Y. & Uchida, S. Evidence for stripe correlations of spins and holes in copper oxide superconductors. *Nature* **375**, 561–563 (1995).
17. Hinkov, V. et al. Electronic liquid crystal state in the high-temperature superconductor $YBa_2Cu_3O_{6.45}$. *Science* **319**, 597–600 (2008).
18. Daou, R. et al. Broken rotational symmetry in the pseudogap phase of a high-$T_c$ superconductor. *Nature* **463**, 519–522 (2010).
19. Lawler, M. J. et al. Intra-unit-cell electronic nematicity of the high-$T_c$ copper-oxide pseudogap states. *Nature* **466**, 347–351 (2010).
20. Fujita, K. et al. Simultaneous transitions in cuprate momentum-space topology and electronic symmetry breaking. *Science* **344**, 612–616 (2014).
21. Achkar, A. J. et al. Nematicity in stripe-ordered cuprates probed via resonant X-ray scattering. *Science* **351**, 576–578 (2016).
22. Sato, Y. et al. Thermodynamic evidence for a nematic phase transition at the onset of the pseudogap in YBa2Cu3Oy. *Nat. Phys.* **13**, 1074–1078 (2017).
23. Wu, J., Bollinger, A. T., He, X. & Bozovic, I. Spontaneous breaking of rotational symmetry in copper oxide superconductors. *Nature* **547**, 432–435 (2017).
24. Kivelson, S. A., Fradkin, E. & Emery, V. J. Electronic liquid-crystal phases of a doped Mott insulator. *Nature* **393**, 550–553 (1998).
25. Wang, S. et al. Discovery of orbital ordering in $Bi_2Sr_2CaCu_2O_{8+x}$. *Nat. Mater.* **23**, 492–498 (2024).
26. Pavarini, E. & Koch, E. *Orbital Physics in Correlated Matter* (Theoretische Nanoelektronik, 2023).
27. Kugel, K. & Khomskii, D. I. Superexchange ordering of degenerate orbitals and magnetic structure of dielectrics with Jahn–Teller ions. *Soviet J. Exper. Theoret. Phys. Lett.* **15**, 446 (1972).
28. Kugel, K. I. & Khomskii, D. I. Crystal-structure and magnetic properties of substances with orbital degeneracy. *Zh. Eksp. Teor. Fiz* **64**, 1429–1439 (1973).
29. Kanamori, J. Crystal distortion in magnetic compounds. *J. Appl. Phys.* **31**, S14–S23 (1960).
30. Krüger, F., Kumar, S., Zaanen, J. & van den Brink, J. Spin-orbital frustrations and anomalous metallic state in iron-pnictide superconductors. *Phys. Rev. B* **79**, 054504 (2009).
31. Lee, C. C., Yin, W. G. & Ku, W. Ferro-orbital order and strong magnetic anisotropy in the parent compounds of iron-pnictide superconductors. *Phys. Rev. Lett.* **103**, 267001 (2009).

32. Lv, W., Wu, J. & Phillips, P. Orbital ordering induces structural phase transition and the resistivity anomaly in iron pnictides. *Phys. Rev. B* https://doi.org/10.1103/PhysRevB.80.224506 (2009).
33. Turner, A. M., Wang, F. & Vishwanath, A. Kinetic magnetism and orbital order in iron telluride. *Phys. Rev. B* https://doi.org/10.1103/PhysRevB.80.224504 (2009).
34. Bascones, E., Calderon, M. J. & Valenzuela, B. Low magnetization and anisotropy in the antiferromagnetic state of undoped iron pnictides. *Phys. Rev. Lett.* **104**, 227201 (2010).
35. Chen, C. C. et al. Orbital order and spontaneous orthorhombicity in iron pnictides. *Phys. Rev. B* https://doi.org/10.1103/PhysRevB.82.100504 (2010).
36. Lv, W., Krüger, F. & Phillips, P. Orbital ordering and unfrustrated(π,0) magnetism from degenerate double exchange in the iron pnictides. *Phys. Rev. B* https://doi.org/10.1103/PhysRevB.82.045125 (2010).
37. Pfau, H. et al. Momentum dependence of the nematic order parameter in iron-based superconductors. *Phys. Rev. Lett.* **123**, 066402 (2019).
38. Yi, M. et al. Symmetry-breaking orbital anisotropy observed for detwinned $Ba(Fe_{1-x}Co_x)_2As_2$ above the spin density wave transition. *Proc. Natl Acad. Sci. USA* **108**, 6878–6883 (2011).
39. Fernandes, R. M., Chubukov, A. V. & Schmalian, J. What drives nematic order in iron-based superconductors? *Nat. Phys.* **10**, 97–104 (2014).
40. Böhmer, A. E., Chu, J.-H., Lederer, S. & Yi, M. Nematicity and nematic fluctuations in iron-based superconductors. *Nat. Phys.* **18**, 1412–1419 (2022).
41. Tokura, Y. & Nagaosa, N. Orbital physics in transition-metal oxides. *Science* **288**, 462–468 (2000).
42. Verwey, E. J. W. Electronic conduction of magnetite ($Fe_3O_4$) and its transition point at low temperatures. *Nature* **144**, 327–328 (1939).
43. He, W., Zeng, W., Yang, T. & Lin, G. Crystal structure of new $R_2TAl_4Ge_2$ (R = Y, Gd–Er, T = Fe, Co) quaternary compounds and magnetic properties of $Gd_2TAl_4Ge_2$. *J. Alloys Compd.* **633**, 265–271 (2015).
44. Huang, K., Sun, Y., Sun, S., Zhang, X. & Lei, H. Physical properties of quaternary compounds $Gd_2CoAl_4T_2$ (T = Si, Ge) single crystals. *Front. Phys.* https://doi.org/10.1007/s11467-018-0870-3 (2018).
45. Yamase, H. Self-masking of spontaneous symmetry breaking in layer materials. *Phys. Rev. Lett.* https://doi.org/10.1103/PhysRevLett.102.116404 (2009).
46. Yamase, H., Oganesyan, V. & Metzner, W. Mean-field theory for symmetry-breaking Fermi surface deformations on a square lattice. *Phys. Rev. B* https://doi.org/10.1103/PhysRevB.72.035114 (2005).
47. Kugel, K. I., Khomskii, D. I., Sboychakov, A. O. & Streltsov, S. V. Spin-orbital interaction for face-sharing octahedra: Realization of a highly symmetric $SU_4$ model. *Phys. Rev. B* **91**, 155125 (2015).
48. Kliment, I. K. & Khomskiĭ, D. I. The Jahn–Teller effect and magnetism: transition metal compounds. *Soviet Phys. Uspekhi* **25**, 231 (1982).
49. Zhang, F. et al. Crystal-symmetry-paired spin–valley locking in a layered room-temperature metallic altermagnet candidate. *Nat. Phys.* **21**, 760–767 (2025).
50. Leonov, I., Yaresko, A. N., Antonov, V. N., Korotin, M. A. & Anisimov, V. I. Charge and orbital order in $Fe_3O_4$. *Phys. Rev. Lett.* **93**, 146404 (2004).
51. Tanaka, A. et al. Symmetry of orbital order in $Fe_3O_4$ studied by Fe L(2,3) resonant X-ray diffraction. *Phys. Rev. Lett.* **108**, 227203 (2012).
52. Khomskii, D. I. & Kugel, K. I. Orbital and magnetic structure of two-dimensional ferromagnets with Jahn-Teller ions. *Solid State Commun.* **13**, 763–766 (1973).
53. Gehring, G. A. & Gehring, K. A. Co-operative Jahn–Teller effects. *Rep. Prog. Phys.* **38**, 1 (1975).





[1]Songshan Lake Materials Laboratory, Dongguan, China. [2]Department of Physics, Southern University of Science and Technology, Shenzhen, China. [3]Beijing National Laboratory for Condensed Matter Physics, and Institute of Physics, Chinese Academy of Sciences, Beijing, China. [4]University of Chinese Academy of Sciences, Beijing, China. [5]Hefei National Laboratory, University of Science and Technology of China, Hefei, China. [6]Department of Physics, University of Science and Technology of China, Hefei, China. [7]Spallation Neutron Source Science Center, Dongguan, China. [8]Institute of High Energy Physics, Chinese Academy of Sciences, Beijing, China. [9]Key Laboratory of Materials Modification by Laser, Ion and Electron Beams (Ministry of Education), School of Physics, Dalian University of Technology, Dalian, China. [10]International School of Microelectronics, Dongguan University of Technology, Dongguan, China. [11]Shanghai Synchrotron Radiation Facility, Shanghai Advanced Research Institute, Chinese Academy of Sciences, Shanghai, China. [12]ALBA Synchrotron, Barcelona, Spain. [13]National Synchrotron Radiation Laboratory, University of Science and Technology of China, Hefei, China. [14]Research Institute for Synchrotron Radiation Science, Hiroshima University, Higashi-Hiroshima, Japan. [15]Institute of Materials Structure Science, High Energy Accelerator Research Organization, Tsukuba, Japan. [16]Institute of Materials Structure Science, High Energy Accelerator Research Organization, Tokai, Japan. [17]These authors contributed equally: Zhanyang Hao, Haohao Sheng, Wanru Ma, Wengen Zheng, Yongqing Cai, Zijuan Xie. ✉e-mail: mwr19@mail.ustc.edu.cn; yqcai@dlut.edu.cn; zywang2@ustc.edu.cn; miaoping@ihep.ac.cn; wzj@iphy.ac.cn; chenchaoyu@sslab.org.cn

# Methods

## Sample growth and characterization

$Tb_2CoAl_4Ge_2$ single crystals were grown by the Al flux method. High-purity Tb (chunks), Co (powder), Al (rods) and Ge (chunks) were mixed in a ratio of 2:1:18:2 and placed into an alumina crucible. The crucible was then placed into a quartz tube and vacuum sealed. The tube was first heated to 1,050 °C and held for 12 h. Then, the temperature was lowered to 750 °C in 150 h and held there for 5 h. Afterwards, the quartz tube was placed into a centrifuge to separate the flux from the single crystals. Millimetre-sized tetragonal single crystals were obtained.

The structure of the crystals was characterized by X-ray diffraction with Cu Kα radiation using a Rigaku Smartlab 9-kW diffractometer. Heat capacity and magnetic susceptibility measurements were performed using Physical Property Measurement System (PPMS) and Magnetic Property Measurement System (MPMS3) of Quantum Design, respectively. In LEED measurements, samples were cleaved in situ under base pressure better than $1 \times 10^{-10}$ mbar and temperature at 35 K. The incident electron energy ranged from 150 to 300 eV, and the sample temperature was varied from 35 to 74 K.

Temperature-dependent high-resolution NPD experiments were conducted on the high-resolution neutron diffractometers TREND of China Spallation Neutron Source[54] and SuperHRPD of Japan Proton Accelerator Research Complex[55]. The powder crystalline samples, ground from the single crystals, were mounted in top-loading cryofurnaces and measured in the temperature range of 3.7–300 K. The collected neutron patterns were analysed using the FELLPROF suite[56] and JANA2020 program[57].

## ARPES measurements

ARPES measurements were performed at the BL03U beamline of the Shanghai Synchrotron Radiation Facility, the BL1 beamline of Research Institute for Synchrotron Radiation Science, the BL13U of National Synchrotron Radiation Laboratory, the LOREA beamline of ALBA Synchrotron, the BL28A beamline of High Energy Accelerator Research Organization and the ID41 beamline of the High Energy Photon Source. The samples were cleaved in situ under base pressure better than $1 \times 10^{-10}$ mbar and temperature below 15 K. The energy resolution was set to 10–20 meV depending on the photon energy used, and the angular resolution was set to 0.2°.

## First-principles calculations

We carried out first-principles calculations based on DFT with the projector-augmented wave method[58,59], as implemented in the Vienna ab initio simulation package (VASP)[60,61]. The generalized gradient approximation in the form of the Perdew–Burke–Ernzerhof (PBE) functional[62] was used for the exchange-correlation potential. The kinetic energy cutoff for the plane-wave expansion was set to 400 eV. The BZ was sampled by the Monkhorst–Pack method in the self-consistent process, with a $10 \times 10 \times 10$ $k$-mesh for non-magnetic phase and a $4 \times 4 \times 2$ $k$-mesh for the AFM phase. The PBE + $U$ method[63] was considered for AFM calculations, where the parameter Hubbard $U$ is selected to be 7 eV for Tb 4$f$ orbitals. The band structure of the AFM phase was obtained using the band unfolding method, as implemented in the VASPKIT package[64]. The maximally localized Wannier functions were constructed using the Wannier90 package[65]. The surface electronic spectra and the Fermi surface were calculated using surface Green's function of the semi-infinite system[66,67], as implemented in the WannierTools package[68].

## Details of mean-field method

As shown in the main text, the two-orbital minimal model of surface states of $Tb_2CoAl_4Ge_2$ reads

$$H_0(k_x,k_y) = m\sigma_0 + A(k_x,k_y)\sigma_0 + B(k_x,k_y)\sigma_z + C(k_x,k_y)\sigma_x,$$

with $A(k_x,k_y) = t_1\left(k_x^2+k_y^2\right) + t_1'\left(k_x^4+k_y^4\right) + t_1''k_x^2k_y^2$, $B(k_x,k_y) = t_2\left(k_x^2-k_y^2\right) + t_2'\left(k_x^4-k_y^4\right)$ and $C(k_x,k_y) = t_3k_xk_y + t_3'\left(k_x^3k_y + k_xk_y^3\right)$. The interaction Hamiltonian we consider is

$$H_{\mathrm{int}} = \frac{S}{2(2\pi)^2}\iint \mathrm{d}^2k\mathrm{d}^2k'\left[f_{kk'}n_k^+n_{k'}^+ - \upsilon n_k^-n_{k'}^-\right].$$

Here, $f_{kk'} = -gd_kd_{k'}$ and $d_k = k_x^2 - k_y^2$. $n_k^\pm = n_{xk} \pm n_{yk}$. $S$ is the area of the unit cell. $g$ and $\upsilon$ are the interaction strengths corresponding to Pomeranchuk instability and ferro-orbital order. $n_{xk}$ and $n_{yk}$ are density operators of $d_{xz}$ and $d_{yz}$ orbitals, respectively. By inserting $n_k = \langle n_k\rangle + \delta n_k$ into the interacting Hamiltonian and neglecting terms of order $(\delta n_k)^2$, we obtain the mean-field Hamiltonian

$$H_{\mathrm{int}}^{\mathrm{MF}} = \int \mathrm{d}^2k\left[\eta d_k n_k^+ + \Delta n_k^-\right] + \frac{(2\pi)^2\eta^2}{2gS} + \frac{(2\pi)^2\Delta^2}{2\upsilon S},$$

where the order parameters are

$$\eta = -\frac{gS}{(2\pi)^2}\int \mathrm{d}^2k d_k\langle n_k^+\rangle,$$

$$\Delta = -\frac{\upsilon S}{(2\pi)^2}\int \mathrm{d}^2k\langle n_k^-\rangle.$$

Here, $\eta$ and $\Delta$ correspond to the $d$-wave Pomeranchuk instability and ferro-orbital order, respectively. The system spontaneously breaks $C_4$ symmetry if either quantity is non-zero. The free energy is as below:

$$F = 2\int \mathrm{d}^2k E_{nk}f_{nk} - \frac{2}{\beta}\int \mathrm{d}^2k\left[f_{nk}\log(f_{nk}) + (1-f_{nk})\log(1-f_{nk})\right] + \frac{(2\pi)^2\eta^2}{2gS} + \frac{(2\pi)^2\Delta^2}{2\upsilon S}.$$

$f_{nk} = f(E_{nk})$ is the Fermi distribution. We solve the mean-field problem self-consistently by using the above formulars and obtain the favoured ferro-orbital order that matches the ARPES results in experiment. Within the framework of our effective two-orbital model, the quantitative free-energy analysis favours the ferro-orbital order scenario over the Pomeranchuk instability. This supports the interpretation that the surface phase transition is driven by orbital order.

## STM measurements

The STM experiments were performed with a commercial CreaTec low-temperature STM system. $Tb_2CoAl_4Ge_2$ single crystals were cleaved under ultrahigh-vacuum conditions ($1 \times 10^{-10}$ torr) at ~30 K and then immediately inserted into the STM head for measurements. The data were acquired at 4.5 K unless otherwise specified, using PtIr tips that were pretreated and calibrated on Au(111) surfaces before measurements. Spectroscopic data were recorded using standard lock-in technique with an a.c. modulation voltage of 1–4 mV at the frequency of 987.5 Hz. The Lawler–Fujita drift-correction algorithm[19] was used to remove the drift effects in the spectroscopic maps, and the resulted FTs are twofold symmetrized to increase the signal-to-noise ratio.

# Data availability

All data are available within the Article and its Supplementary Information. Further data are available from the corresponding author on reasonable request. Source data are provided with this paper.

# References

54. Tan, Z. et al. Radial collimator with ultra-wide scattering angle coverage for high-resolution neutron diffractometer TREND. *Nucl. Instrum. Methods Phys. Res. A* **1083**, 171096 (2026).

55. Torii, S. et al. Super high resolution powder diffractometer at J-PARC. *J. Phys. Soc. Jpn* **80**, SB020 (2011).
56. Rodríguez-Carvajal, J. Recent advances in magnetic structure determination by neutron powder diffraction. *Physica B* **192**, 55–69 (1993).
57. Petříček, V., Palatinus, L., Plášil, J. & Dušek, M. Jana2020—a new version of the crystallographic computing system Jana. *Z. Kristallogr. Cryst. Mater.* **238**, 271–282 (2023).
58. Blöchl, P. E. Projector augmented-wave method. *Phys. Rev. B* **50**, 17953–17979 (1994).
59. Kresse, G. & Joubert, D. From ultrasoft pseudopotentials to the projector augmented-wave method. *Phys. Rev. B* **59**, 1758–1775 (1999).
60. Kresse, G. & Furthmüller, J. Efficient iterative schemes for ab initio total-energy calculations using a plane-wave basis set. *Phys. Rev. B* **54**, 11169–11186 (1996).
61. Kresse, G. & Furthmüller, J. Efficiency of ab-initio total energy calculations for metals and semiconductors using a plane-wave basis set. *Comput. Mater. Sci* **6**, 15–50 (1996).
62. Perdew, J. P., Burke, K. & Ernzerhof, M. Generalized gradient approximation made simple. *Phys. Rev. Lett.* **77**, 3865–3868 (1996).
63. Vladimir, I. A., Aryasetiawan, F. & Lichtenstein, A. I. First-principles calculations of the electronic structure and spectra of strongly correlated systems: the LDA + U method. *J. Phys. Condens. Matter* **9**, 767 (1997).
64. Wang, V., Xu, N., Liu, J.-C., Tang, G. & Geng, W.-T. VASPKIT: a user-friendly interface facilitating high-throughput computing and analysis using VASP code. *Comput. Phys. Commun.* **267**, 108033 (2021).
65. Pizzi, G. et al. Wannier90 as a community code: new features and applications. *J. Phys. Condens. Matter* **32**, 165902 (2020).
66. Sancho, M. P. L., Sancho, J. M. L. & Rubio, J. Quick iterative scheme for the calculation of transfer matrices: application to Mo (100). *J. Phys. F* **14**, 1205 (1984).
67. Sancho, M. P. L., Sancho, J. M. L., Sancho, J. M. L. & Rubio, J. Highly convergent schemes for the calculation of bulk and surface Green functions. *J. Phys. F* **15**, 851 (1985).
68. Wu, Q., Zhang, S., Song, H.-F., Troyer, M. & Soluyanov, A. A. WannierTools: an open-source software package for novel topological materials. *Comput. Phys. Commun.* **224**, 405–416 (2018).


## Acknowledgements

We acknowledge the Center for Materials Genome, the neutron beam time at TREND (Shenzhen Guangming Science City Development and Construction. and its Material Genome Big-Science Facilities Platform, https://cstr.cn/31113.02.CSNS.TREND) of CSNS (https://cstr.cn/31113.02.CSNS), as well as the assistance in ARPES measurements from the Shanghai Synchrotron Radiation Facility (SSRF) of BL03U (grant number 31124.02.SSRF.BL03U) and the ID41-High Resolution Nanoscale Electronic Structure Spectroscopy Beamline of High Energy Photon Source (https://cstr.cn/31138.02.HEPS.ID41).

## Author contributions

C.C. conceived and supervised the research. Z.H., Y.C., W.Z., C.L., Z.L., M.Y., J.D., M.T., S.C., Y.K., K.S., K.O. and J.W. contributed to the ARPES instruments, measurement and analysis. Z.H., Y.C., Z.X., Z.S., J.M., J.L. and L.W. contributed to the sample growth and characterization. Y.C., Z.S., X.Z., and J.G. performed LEED measurements and analysis. W.Z., W.X., S.T., K.M. and P.M. performed the NPD measurements and analysis. H.S., Y.X., J.D. and Z.W. performed calculations/simulations. W.M., W.C., Z.Y.W. and X.C. performed the STM measurements and analysis. All authors wrote and corrected the paper.

## Funding

This work is supported by the National Key R&D Program of China (grant numbers 2022YFA1403700 to C.C., 2022YFA1403800 to Z.W. and 2025YFA1411200 to C.C.), the National Natural Science Foundation of China (NSFC) (grant numbers 12574068 to C.C. and 12188101 to Z.W.), Guangdong Major Project of Basic Research (grant number 2026B0303000004 to C.C.), Guangdong Basic and Applied Basic Research Foundation (grant numbers 2022B1515020046 to C.C., 2022B1515130005 to C.C., 2021B1515130007 to C.C., 2022B1515120014 to P.M., 2023B0303000003 to P.M. and 2023B1515120060 to P.M.), the Guangdong Innovative and Entrepreneurial Research Team Program (grant numbers 2019ZT08C044 to C.C. and 2021ZT09C539 to P.M.), Shenzhen Science and Technology Program (grant number KQTD20190929173815000 to C.C.).

## Competing interests

The authors declare no competing interests.

## Additional information

**Extended data** is available for this paper at https://doi.org/10.1038/s41567-026-03359-4.

**Supplementary information** The online version contains supplementary material available at https://doi.org/10.1038/s41567-026-03359-4.

**Correspondence and requests for materials** should be addressed to Wanru Ma, Yongqing Cai, Zhenyu Wang, Ping Miao, Zhijun Wang or Chaoyu Chen.

**Peer review information** *Nature Physics* thanks the anonymous reviewer(s) for their contribution to the peer review of this work. Peer reviewer reports are available.

https://doi.org/10.1038/s41567-026-03359-4

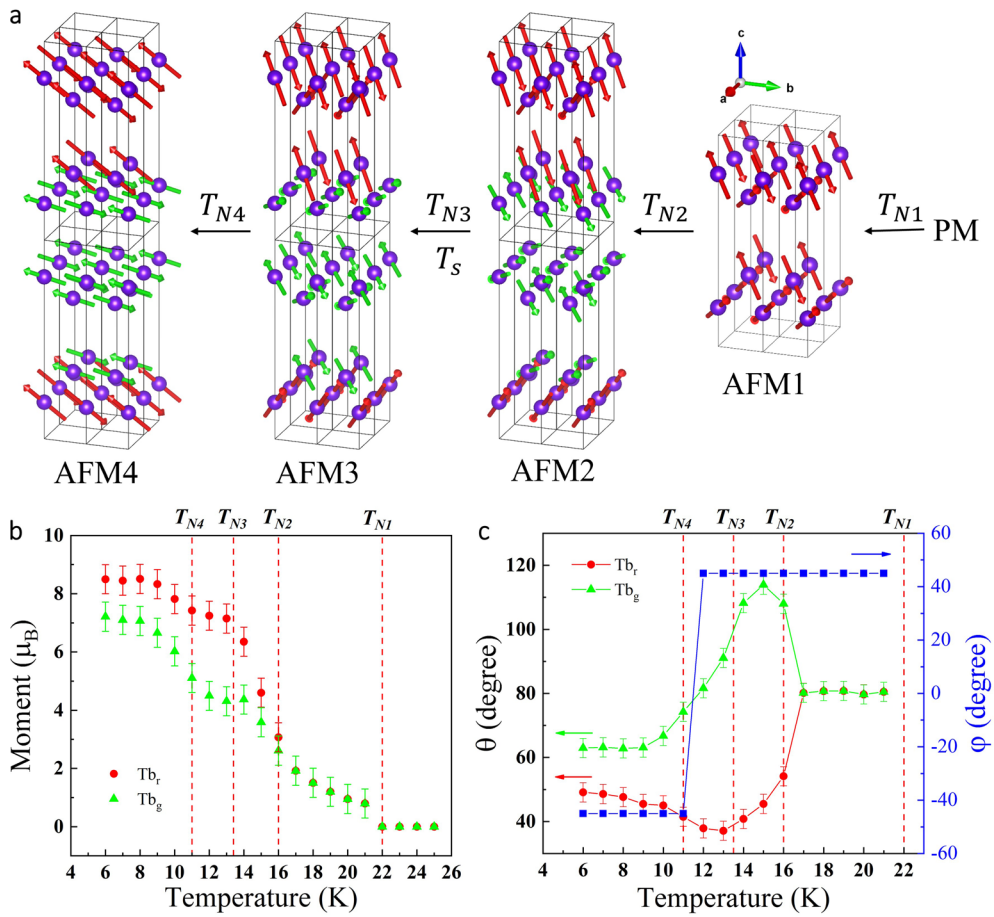


**Extended Data Fig. 1 | Magnetic structures of Tb2CoAl4Ge2. a**, Green and red arrows represent two types of moments with different magnitudes along the *c*-axis due to the influence of $k_2$. The *c*-axis components of the green moments are smaller than those of the red ones, while their components along the *a*- and *b*-axes are identical. **b-c**, Temperature dependence of magnitude (**b**) and angles (**c**) of Tb moments. Tb$_r$ and Tb$_g$ indicate the red and green moments in (**a**). $\theta$ denotes the angle between the moment and the *c*-axis, while $\varphi$ represents the angle between the projection of the moment on *ab*-plane and the *a*-axis. Error bars indicate the tolerance range of the refined parameter; adding such variation does not noticeably change the goodness-of-fit of the refinement.

https://doi.org/10.1038/s41567-026-03359-4

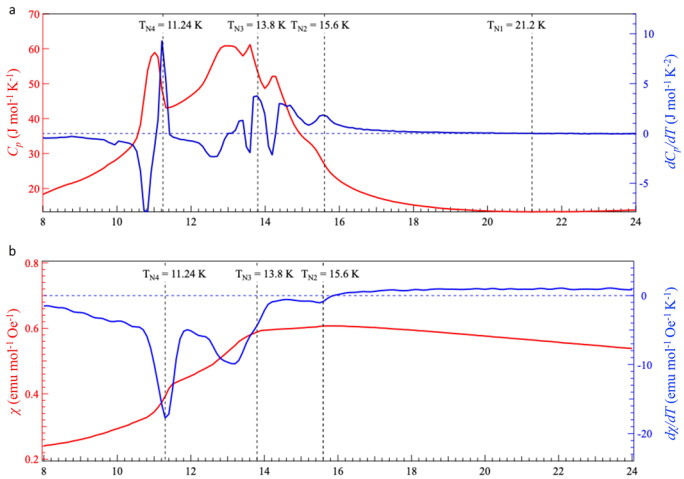


**Extended Data Fig. 2 | Defining AFM transition temperatures from heat capacity and susceptibility curves of Tb2CoAl4Ge2. a-b**, Red solid lines represent the measured heat capacity $C_p$ (**a**) and susceptibility $\chi$ (**b**) while blue solid lines are the corresponding temperature derivatives. By comparing the line shapes of all the 4 curves to the NPD results, we were able to define 4 transition temperatures charactering the AFM transition. From high-temperature to low-temperature, $T_{N1} = 21.2$ K represents a slope change of $C_p$ from negative to positive, $T_{N2} = 15.6$ K and $T_{N4} = 11.24$ K mark local maxima in $dC_p/dT$ and minima in $d\chi/dT$. $T_{N3} = 13.8$ K marks a local maximum in $dC_p/dT$ and a kink in $\chi$.

https://doi.org/10.1038/s41567-026-03359-4

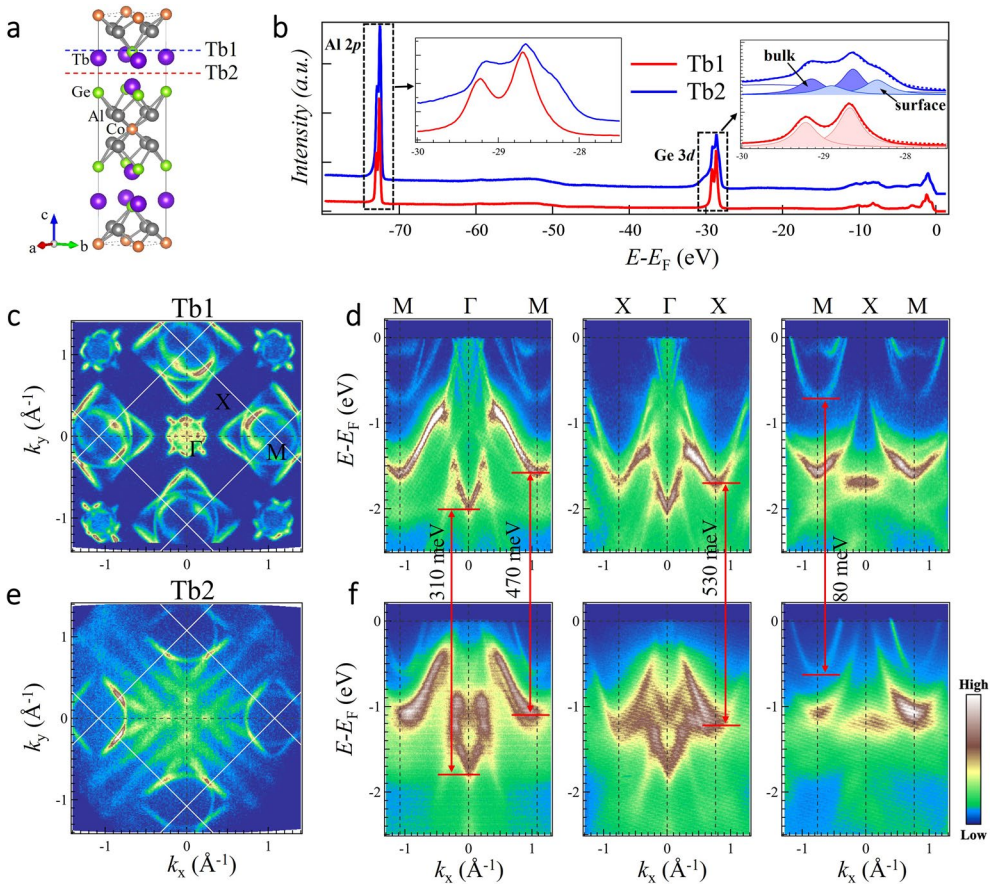


**Extended Data Fig. 3 | Termination-dependent electronic structure in Tb2CoAl4Ge2. a**, Schematic of two terminations Tb1 and Tb2. **b**, XPS spectra of *in-situ* cleaved surface, showing two distinct terminations: Tb1 (red) and Tb2 (black). The inset highlights the Al 2p and Ge 3d core levels. For the Ge 3d doublets, the Tb1 termination exhibits two peaks, while the Tb2 termination shows that each spin-orbit component splits into two peaks—a higher-binding-energy peak originating from bulk Ge atoms and a lower-binding-energy peak from surface Ge atoms. **c**, Fermi surface mapping of Tb1 termination. **d**, ARPES spectra of Tb1 termination taken along high symmetry direction M-Γ-M, X-Γ-X and M-X-M. **e-f**, Same as (**c-d**) but for Tb2 terminations. Note that the energy shift between the two terminations is band-dependent and not a rigid shift. All ARPES data in (**c-f**) were acquired with a photon energy of 119 eV.

https://doi.org/10.1038/s41567-026-03359-4

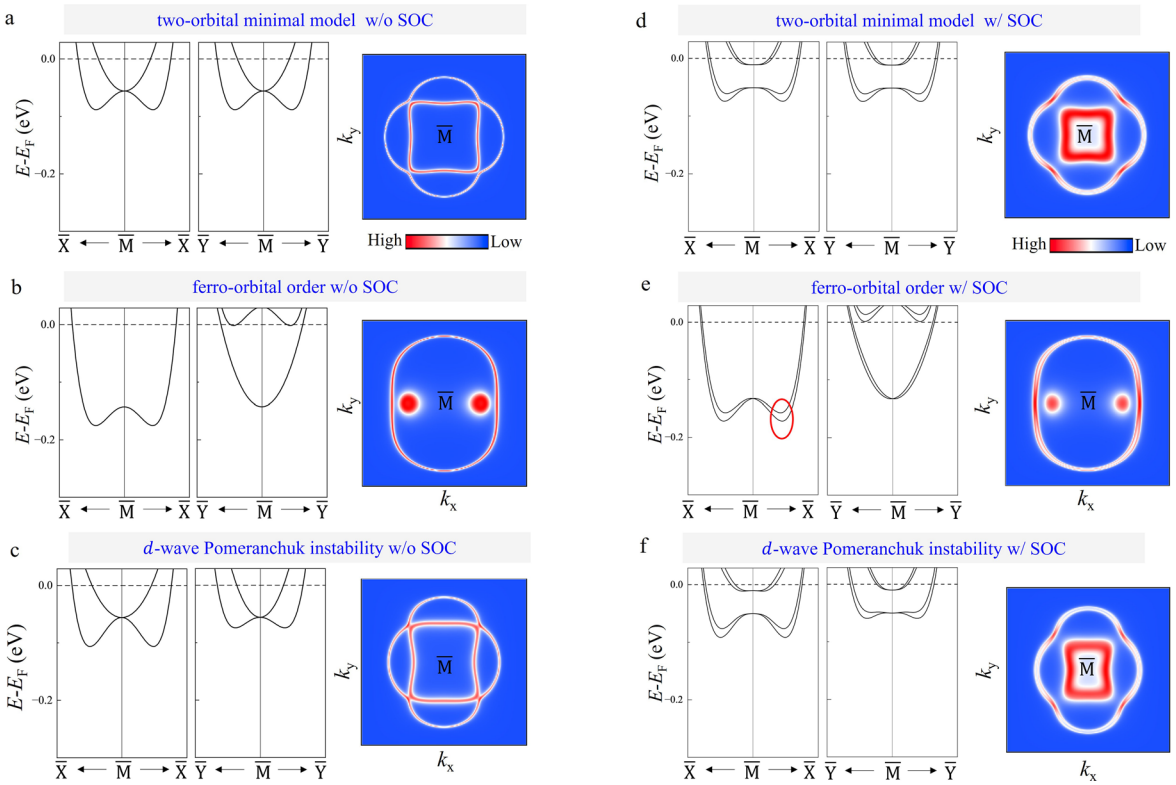


**Extended Data Fig. 4 | Mean-field results with and without SOC. a**–**c**, Band dispersion and Fermi surface (**a**) without order, (**b**)with ferro-orbital order and (**c**) with Pomeranchuk instability, without SOC. **d**–**f**, like (**a**-**c**), but with SOC.

https://doi.org/10.1038/s41567-026-03359-4

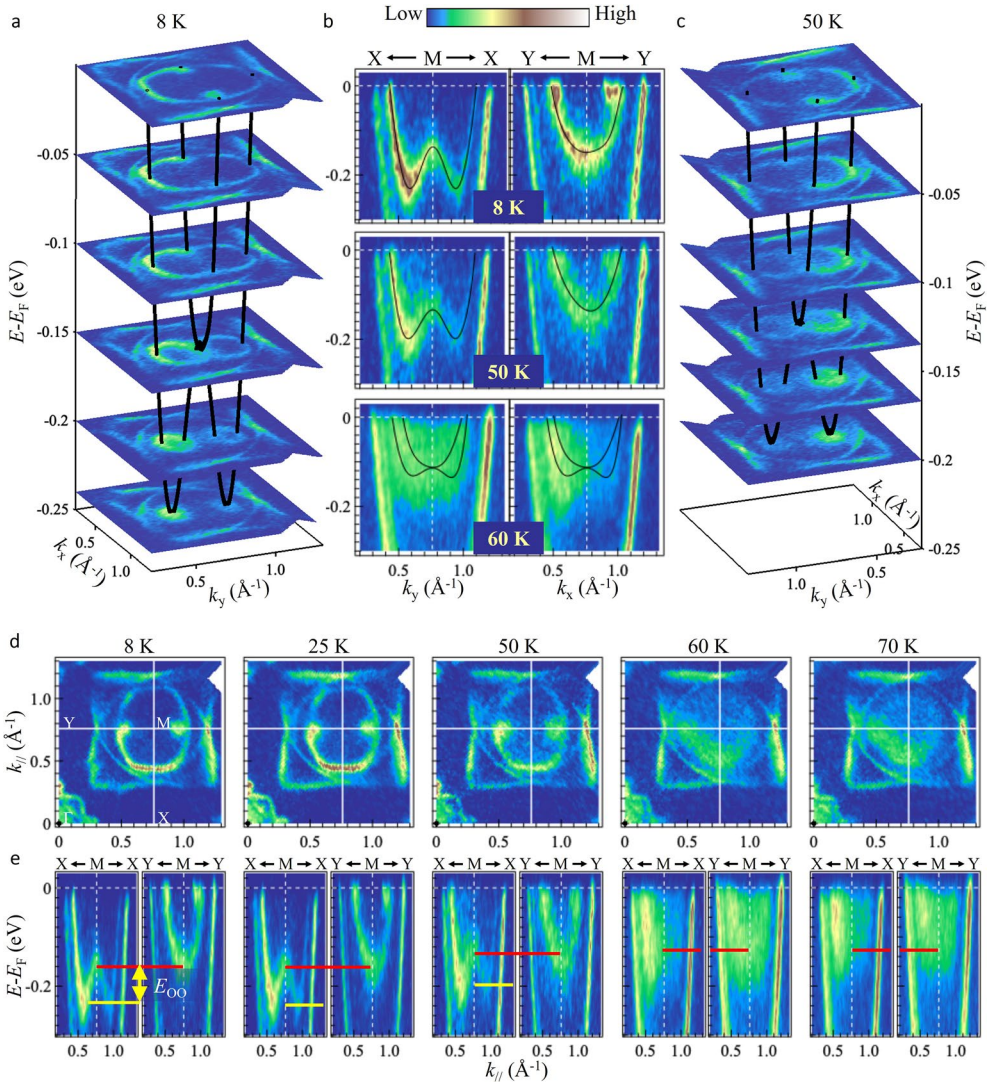


**Extended Data Fig. 5 | Temperature dependence of the surface state anisotropy energy $E_{OO}$. a,c**, ARPES intensity in $E_B - k_x - k_y$ space at 8 K (**a**) and 50 K (**c**), respectively. **b**, ARPES spectra along X − M − X (left) and Y − M − Y (right) direction at 8 K (top), 50 K (middle) and 60 K (bottom). Black solid lines represent extracted surface state dispersions. **d**, ARPES Fermi surface measured at various temperatures. **e**, Corresponding spectra along X-M-X and Y-M-Y. Red lines indicate the saddle points at M while green lines for the band bottom of the W-shaped surface bands. The anisotropy energy $E_{OO}$ is defined as their energy difference.

https://doi.org/10.1038/s41567-026-03359-4

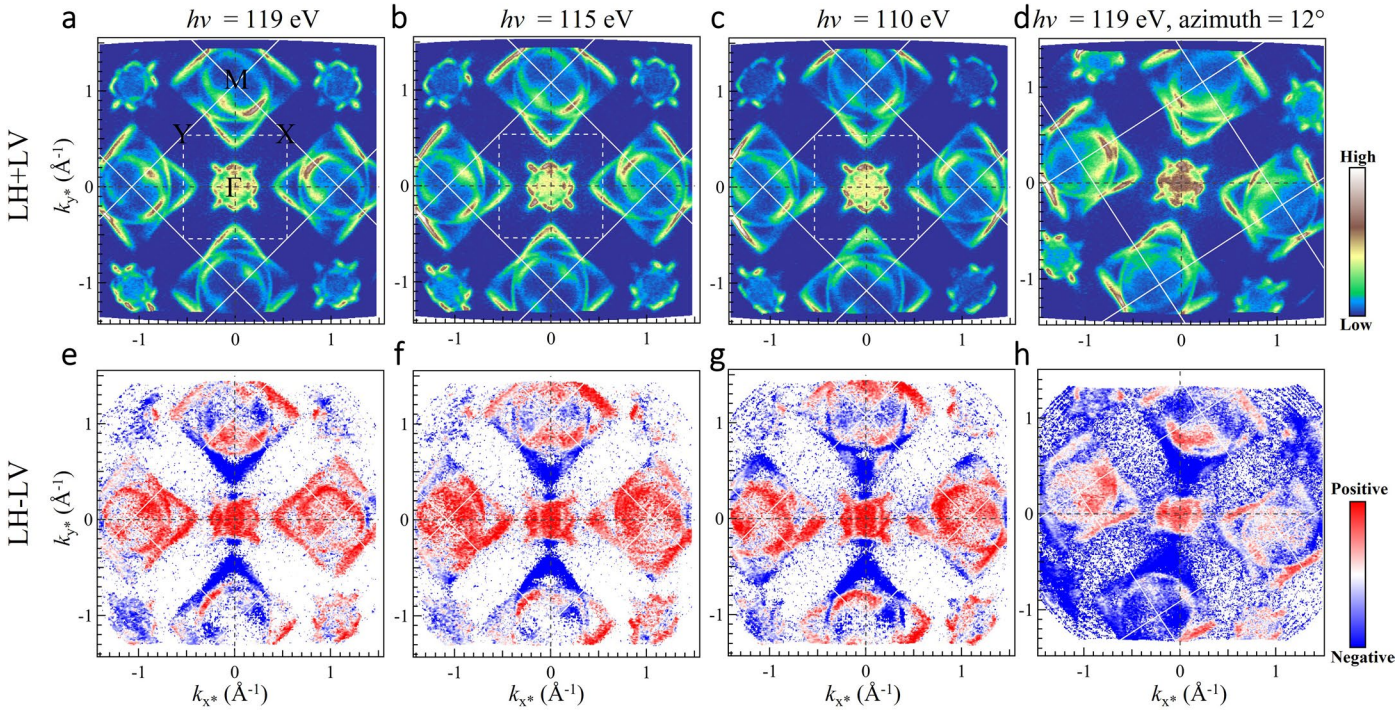


**Extended Data Fig. 6 | Photon-energy- and geometry-dependent orbital polarization of Tb2CoAl4Ge2. a-c**, ARPES Fermi surface maps obtained by summing the photoemission intensity from LH and LV polarizations at photon energies of 119 eV (**a**), 115 eV (**b**), and 110 eV (**c**). **d**, Same as (**a**) but with the sample azimuthally rotated by 12°. **e-h**, Corresponding LD Fermi surface maps (LH − LV) of (**a-d**). The observed dichroism pattern, negative along $k_{y*}$ and positive along $k_{x*}$, remains robust against photon energy variation and azimuthal rotation, ruling out final-state effects and geometry as its origin and confirming the intrinsic orbital polarization of the surface state.

https://doi.org/10.1038/s41567-026-03359-4

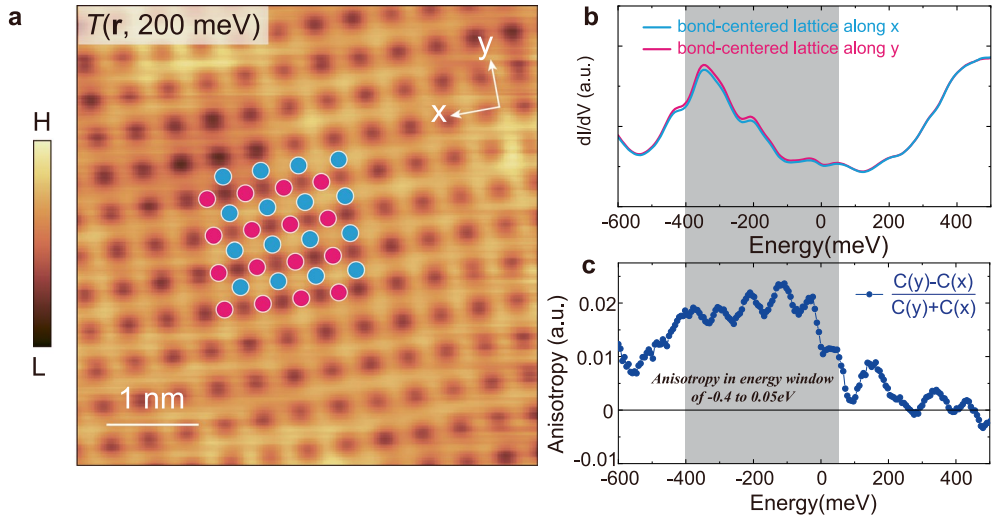


**Extended Data Fig. 7 | Site-dependent dI/dV spectroscopy. a**, Topographic image on the Tb1 termination. As the $C_2$ pattern aligns along one of the Tb1-Tb1 bonds, it naturally defines two inequivalent bond centers along *x* and *y* directions. The red and blue dots denote 4×4 grids for the *x* and *y* bond centers where dI/dV spectra were collected. **b**, The dI/dV spectra averaging from these 16 sites for each grid. **c**, Anisotropy ratio of the averaging spectra, which mainly develops in the energy window of −0.4 to 0.05 eV. Setup conditions: tunnelling current $I_t$ = 3 nA (**a**).

https://doi.org/10.1038/s41567-026-03359-4

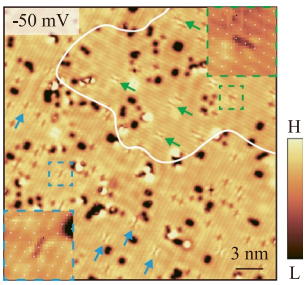


**Extended Data Fig. 8 | Nematic domains.** Topographic image acquired at -50mV showing nematic domains on the Tb1 surface. The electronic structures near Tb1 vacancies (labelled by blue and green arrows) are $C_2$ symmetry and share the same $C_2$ orientation within a single domain. When crossing the domain boundary, both the stripe modulation and the $C_2$ electronic states near Tb1 vacancies rotate by 90°. The insets show the zoom-in of the defects. Setup conditions: tunnelling current $I_t$ = 500 pA.

https://doi.org/10.1038/s41567-026-03359-4

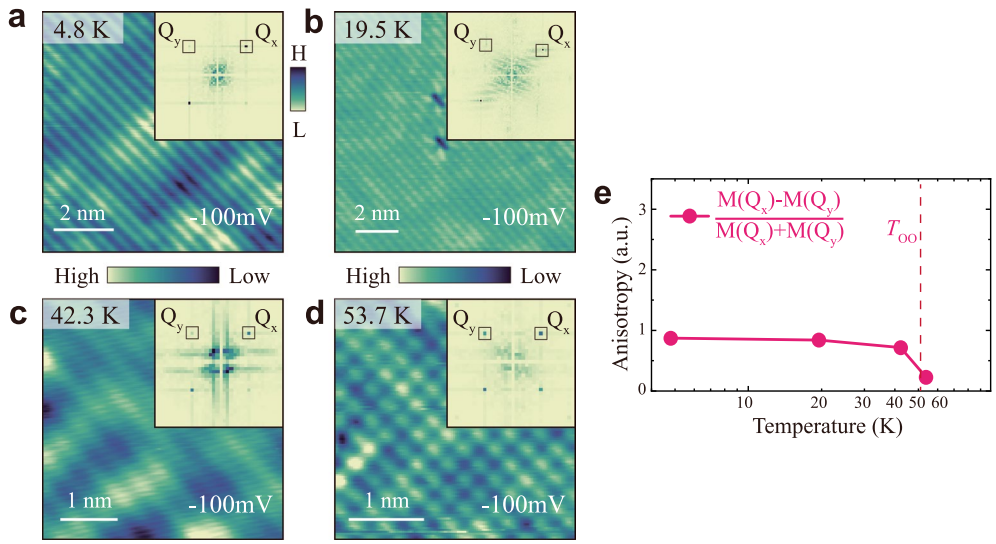


**Extended Data Fig. 9 | Temperature-dependent STM topography and anisotropy. a-d**, Topographic images obtained at -100mV at different temperatures. The insets show their Fourier transforms after drift-corrections. To quantify, we define a ratio of amplitudes at the wave vector of the lattice, $(M(Q_x)-M(Q_y))/(M(Q_x)+M(Q_y))$. The result is shown in **e** as a function of temperature, showing that the anisotropy is significantly suppressed at around 51 K. Setup conditions: tunnelling current $I_t = 2$ nA (**a**), $I_t = 300$ pA (**b**), $I_t = 1.1$ nA (**c**), $I_t = 400$ pA (**d**).

https://doi.org/10.1038/s41567-026-03359-4

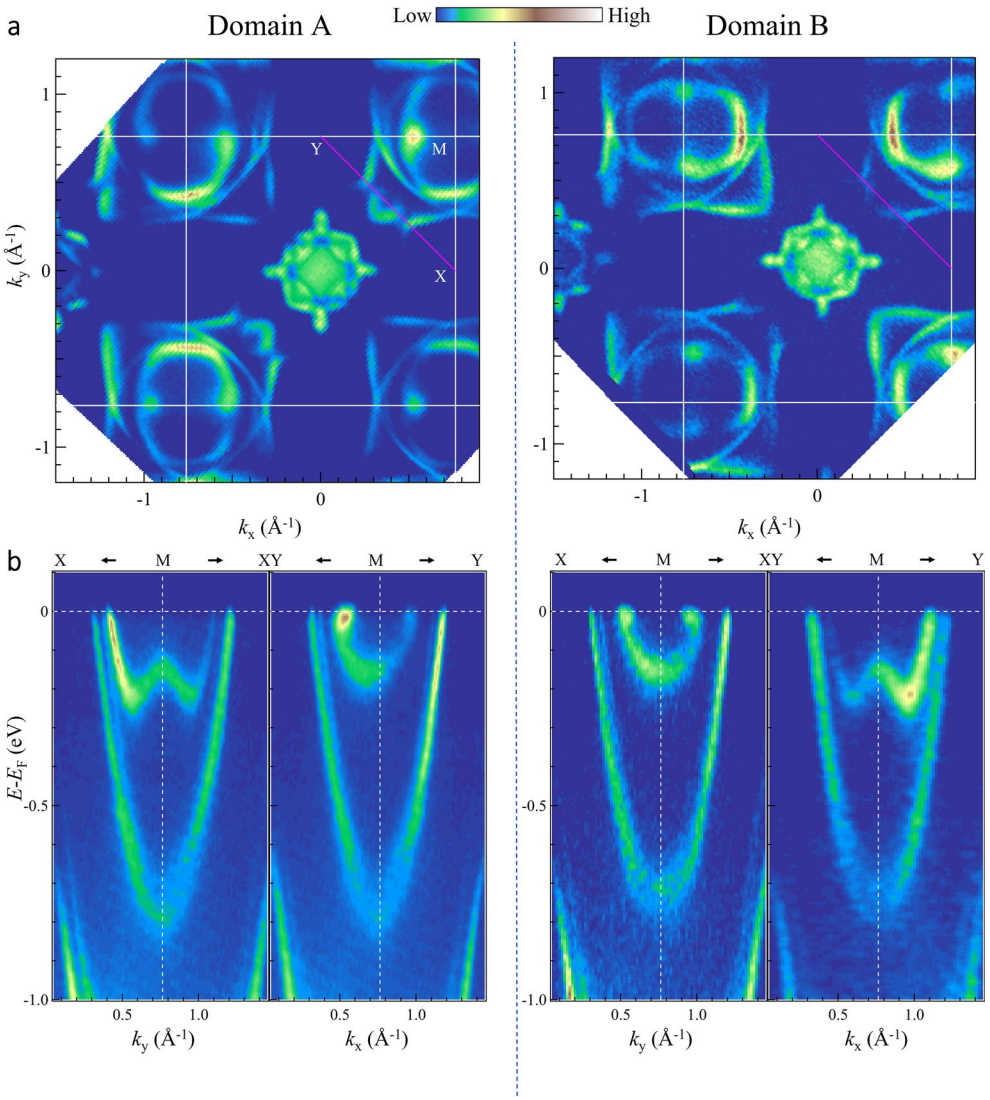


**Extended Data Fig. 10 | Domain dependence of the surface state Fermi surface and spectra. a**, Fermi surfaces measured at Domain **A** (left panel) and **B** (right panel) at temperature 7 K. Pink line indicates the mirror plane with respect to which the dominant band folding occurs. While both domains show clear SDW-type band folding features along ($\pi$, $\pi$) direction, the surface state nematicity is rotated by 90° from domain A to domain B. **b**, The corresponding ARPES spectra along X-M-X and Y-M-Y directions, showing the surface dispersion features are also switched between $k_y$ and $k_x$. All ARPES data were acquired with a photon energy of 119 eV.